Shadow Removal and Contrast Enhancement in Optical Coherence Tomography Images of the Human Optic Nerve Head

Michaël J. A. Girard,[1] *Nicholas G. Strouthidis,*[2] *C. Ross Ethier,*[1] *and Jean Martial Mari*[1,3]

Purpose. To improve the quality of optical coherence tomography (OCT) images of the optic nerve head (ONH).

Methods. Two algorithms were developed, one to compensate for light attenuation and the other to enhance contrast in OCT images. The former was borrowed from developments in ultrasound imaging and was proven suitable with either time- or spectral-domain OCT. The latter was based on direct application of pixel intensity exponentiation. The performances of these two algorithms were tested on spectral-domain OCT images of four adult ONHs.

Results. Application of the compensation algorithm significantly reduced the intralayer contrast (from 0.74 ± 0.16 to 0.17 ± 0.12; $P < 0.001$), indicating successful blood vessel shadow removal. Furthermore, compensation dramatically improved the visibility of deeper ONH tissues, such as the peripapillary sclera and lamina cribrosa. Application of the contrast-enhancement algorithm significantly increased the interlayer contrast (from 0.48 ± 0.22 to a maximum of 0.89 ± 0.05; $P < 0.001$) and thus allowed a better differentiation of tissue boundaries. Contrast enhancement was robust only when compensation was considered.

Conclusions. The proposed algorithms are simple and can significantly improve the quality of ONH images clinically captured with OCT. This study has important implications, as it will help improve our ability to perform automated segmentation of the ONH; quantify the morphometry and biomechanics of ONH tissues in vivo; and identify potential risk indicators for glaucoma. (*Invest Ophthalmol Vis Sci.* 2011;52:7738–7748) DOI:10.1167/iovs.10-6925

Glaucoma is the second most common cause of blindness worldwide[1] and leads to vision loss by damaging retinal ganglion cell axons in and around the optic nerve head (ONH).[2] Although the underlying causes are likely to be multifactorial,[3] ample evidence now suggests that glaucoma is a biomechanically related disorder and that ONH biomechanics is an important driving mechanism.[4–7] However, quantifying ONH biomechanics is complex, and so far investigators have used analytical[8–10] or computational models.[11–15] Although such models perform well, they have relied solely on ex vivo measurements; thus, they have poor predictive capabilities in a clinical setting and are not appropriate for glaucoma diagnosis, prognosis, and risk profiling. To achieve clinical utility, in vivo measurements of the geometry and the mechanical properties of all tissues within the ONH, as well as the load (i.e., intraocular pressure, IOP) that acts on them, are required, which can then be used in patient-specific biomechanical models of the ONH.

Optical coherence tomography (OCT) has the potential to be a powerful tool for quantification of the in vivo biomechanics of the ONH. OCT is a noninvasive imaging technology that is already widely used in the clinical setting. The newest generation of spectral domain OCT devices can acquire serial B-scans rapidly (40,000+ A-scans/second), yielding 3D volumes of the ONH with an axial resolution of approximately 4 μm for commercial devices, improving to 1 μm for experimental ultrahigh-resolution devices.[16] The depth of light penetration of commercially available spectral domain OCT scanners is now sufficient to start visualizing and identifying the structures of the lamina cribrosa (LC) and the adjacent peripapillary sclera (PS),[17,18] both of which are thought to strongly influence ONH biomechanics.[19–24]

However, despite the improved axial resolution and increased depth penetration, there are some limitations to using OCT to target these deep ONH structures, which may result in clinical misinterpretation and morphometric (parameterization) errors. Although an ability to visualize the full thickness of the LC has been reported in human subjects,[25] a histologic comparison using a normal monkey ONH failed to clearly identify the posterior surface of the LC.[17] It is our experience that the ability to distinguish the anterior and posterior boundaries of the LC and indeed the PS is highly variable between subjects. The principal reason for failing to visualize these deep structures is the shadows cast by blood vessels, in particular those arising from the central retinal vessel trunk. Furthermore, as incident light travels through the ONH, it attenuates with depth, such that reflected signals from deep structures may be too weak to be reliably detected.

To address these problems, we consider herein the OCT imaging process itself, in which a light wave is transmitted to the specimen to be imaged, which in turn backscatters (or reflects back to the source) a fraction of the incident light toward a detector for manipulation, measurement, and processing. OCT is thus categorized as a pulse–echo imaging technique, along with radar,[26] sonar,[27] and ultrasound.[28] Although the latter three techniques have benefited from substantial improvements in both hardware (for transmission and reception) and software (for image enhancement),[29–31] medical OCT applications are still adversely affected by strongly scattering and attenuating structures (e.g., pigment and blood).

From the [1]Department of Bioengineering, Imperial College, London, United Kingdom; [2]NIHR (National Institute of Health Research) Biomedical Sciences Centre, Moorfields Eye Hospital and UCL Institute of Ophthalmology, London, United Kingdom; and [3]INSERM (Institut National de la Santé et de la Recherche Médicale) U556, Lyon, France; and Université de Lyon, Lyon, France.

Supported by an Imperial College Junior Research Fellowship (MJAG) Royal Society Wolfson Research Excellence Award (CRE).

Submitted for publication November 20, 2010; revised April 6, 2011; accepted April 22, 2011.

Disclosure: **M.J.A. Girard**, None; **N.G. Strouthidis**, None; **C.R. Ethier**, None; **J.M. Mari**, None

Corresponding author: Michaël J. A. Girard, Department of Bioengineering, Imperial College London, South Kensington Campus, London SW7 2AZ, UK; m.girard@imperial.ac.uk.

Since our ultimate goal is to measure morphometric and biomechanical parameters of the ONH, it is crucial to obtain high-quality images of the ONH. Thus, in this study, we sought to develop algorithms to improve the quality of OCT images. In so doing, we hope that these improvements will enhance our ability to segment these images and to perform more accurate quantitative morphometry, eventually thus serving as the basis for novel diagnosis and risk profiling in glaucoma.

Chang et al.[32] recently proposed a method of correcting light attenuation in OCT images through exponential decay modeling of the A-scan pixel intensity across biological layers, using images from three different nonocular biosamples acquired with an experimental swept-source OCT device. This approach is not very suitable for the ONH or the macula, both of which are composed of many thin sublayers with varying attenuation. Uniform processing of the signals from these different sublayers can overestimate the local attenuation. Furthermore, the technique of Chang et al. interprets all decreasing intensity with depth as attenuation, while deeper layers could simply cause less scattering and would benefit from an appropriate local analysis.

Hughes and Duck[33] developed an approach to correcting sound attenuation for ultrasound imaging that allows the adaptive amplification of the pulse–echo signals with depth—a process called time-gain compensation, or simply compensation. The technique works only when the local amount of backscattering can be related to that of the corresponding attenuation, which is usually the case when other local sources of degradation of the pulse–echo signals can be neglected.

Considering the analogy between sound and light, The compensation approach of Hughes and Duck[33] could be applied to OCT to correct light attenuation. To this end, we defined and introduced an attenuation term in the governing OCT equations. Then an analogy was made with their compensation technique, and the corresponding compensation equations were rederived for OCT. Furthermore, we proposed a series of contrast-enhancement techniques, which have strong potential to facilitate segmentation through better detection of ONH tissue boundaries.

Materials and Methods

Few studies have introduced an attenuation term in the governing OCT equations,[32] and fewer have tried to compensate for attenuation,[34] although it has been suggested.[35] The absence of such a term compromises the automated interpretation of the OCT images and prevents the application of contrast enhancement techniques, which can facilitate boundary detection through segmentation. In the first section of the article, an attenuation term is introduced into the governing OCT equations, and the pulse–echo compensation approach described by Hughes and Duck is used, to show that it can be applied to OCT images. In the second section, a basic square expansion (also referred to as exponentiation) is applied to the OCT images at different steps in the compensation process for contrast-enhancement purposes.

Blood Vessel Shadow Removal

OCT Theory. In the standard spectral-domain OCT modeling approach, the detected photocurrent I_D of the interference between a light beam reflected from a reference mirror (with electric field $E_R = \frac{E_i}{\sqrt{2}} e^{i2kz_R}$) and that from a sample of interest (with electric field $E_S = \int_{z_0}^{\infty} \frac{E_i}{\sqrt{2}} r_S(z) e^{i2kz} dz$), is described in its continuous form by

$$= \frac{\rho}{2}\left\langle \left| E_R + E_S \right| \right\rangle = \frac{\rho}{2} S(k) \left[\underbrace{A}_{\text{Constant Offset}} + \underbrace{\int_{z_0}^{+\infty} r_S(z) cos[2k(z_R - z)] dz}_{\text{B = Cross-correlation}} + \underbrace{C}_{\text{Auto-correlation}} \right] \quad (1)$$

where E_i is the electric field from the incoming light source; S is the light source spectrum; z_R is the distance between the mirror and the beam splitter; z is the sample depth with respect to the beam splitter; z_0 is the anterior boundary of the sample; r_S is the sample reflectivity; k is the wave number; and ρ is the responsivity of the OCT detector. It is noted that equation 1 is further manipulated (through an inverse Fourier transform) to isolate the sample reflectivity r_S, the quantity that forms an OCT A-scan when considered as a function of depth, z.[36] However, a limitation of equation 1 is that it assumes the light does not attenuate while propagating, which is equivalent to assuming that light propagates through the full depth of the sample, so that full-depth imaging without any blood vessel shadowing is achievable. To overcome this limitation, we modified equation 1 by taking into account light attenuation.

Attenuation. When light penetrates the sample, a relatively small portion of it is converted into heat through absorption while the rest scatters in all directions. Depending on the light's wavelength and the local scattering properties of the sample, different models can be used to describe the scattered light.[37] Assuming that the same scattering model can be used for each sublayer and that heat conversion can be neglected, the quantity scattered locally from the forward-propagating beam can be considered to be proportional to the local backscattering, which in turn is a function of the local reflectivity r_S. In other words, the local attenuation is entirely dependent on the local scattering, and for each sample layer, a constant fraction of the scattered beam is assumed to be retropropagated in the direction of observation. Therefore, the local attenuation of the propagating beam a_S at depth z can be assumed to be proportional to the local reflectivity r_S as described by

$$a_S(z) = \alpha r_S(z) \quad (2)$$

where α is a proportionality coefficient. Accordingly, the attenuated propagating electric field E_{ia} can be expressed as

$$E_{ia}(z) = E_i e^{-\int_{z_0}^{z} a_S(u)du} = E_i e^{-\alpha \int_{z_0}^{z} r_S(u)du} \quad (3)$$

which now replaces E_i in E_S, giving

$$E_S = \int_{z_0}^{\infty} \frac{E_i}{\sqrt{2}} r_S(z) e^{-\alpha \int_{z_0}^{z} r_S(u)du} e^{i2kz} dz. \quad (4)$$

When equation 4 is introduced into the governing OCT equation 1, the attenuated cross-correlation term B_a becomes

$$B_a = \int_{z_0}^{\infty} r_S(z) e^{-2\alpha \int_{z_0}^{z} r_S(u)du} \cos[2k(z_R - z)]dz. \quad (5)$$

By analogy with the cross-correlation term B in equation 1, equation 5 shows that standard spectral-domain OCT postprocessing does not extract the reflectivity profile r_S to form an A-scan, but instead its attenuated version $r_S(z)e^{-2\alpha \int_{z_0}^{z} r_S(u)du}$, which is why shadows appear behind strongly attenuating structures such as blood vessels and pigment. To correct the attenuation and thus remove the shadows from the OCT images, the decay term $e^{-2\alpha \int_{z_0}^{z} r_S(u)du}$ must be removed; this step is called compensation.

Compensation in Ultrasound. The introduction of an attenuation term in the OCT equation 5 which is proportional to the local reflectivity emphasizes the fact that the OCT imaging process is a type of progressively attenuated pulse–echo imaging. For such imaging, an automatic compensation technique has been developed by Hughes and Duck[33] under assumptions that fit the present OCT case extremely well. In their model, an ultrasound beam is transmitted along a path, and the pressure pulse (the sound analogy of the electric field for light) is progressively attenuated by the local scattering due to tissue inhomogeneities and degradation. They further assumed that the local attenuation is proportional to the local backscattering and neglected the other degradation processes. Under this assumption, they developed a model for the propagating beam and the resulting measured ultrasound signal, which allows the design of an automatic compensation method, as follows

$$R(z) = \mu \cdot b(z) \cdot \underbrace{P_0 e^{-\beta \int_{z_0}^{z} b(u)du}}_{P(z)} \cdot e^{-\beta \int_{z_0}^{z} b(u)du} = \mu P_0 b(z) \underbrace{e^{-2\beta \int_{z_0}^{z} b(u)du}}_{\text{decay term}}, \quad (6)$$

where $P(z)$ is the propagating ultrasound pressure pulse with initial value P_0; $b(z)$ is the local backscattering coefficient; β is a coefficient such that $\beta b(z)$ is the corresponding local attenuation; μ is a piezoelectric coefficient of conversion; and $R(z)$ is the attenuated signal amplitude detected by the ultrasound scanner. Under such conditions, Hughes and Duck showed that the attenuation profile $\beta b(z)$ can be separated from the decay term in equation 6 according to

$$\beta b(z) = \frac{R(z)}{2\int_{z}^{\infty} R(u)du}. \quad (7)$$

A strength of the Hughes and Ducks approach is the ability to extract a tissue intrinsic property (the attenuation profile $\beta b(z)$) without requiring estimation of the model's parameters (β and μ). This technique matches the situation in standard OCT, allowing automatic compensation equations to be derived, as follows.

Compensation in OCT. Assuming that the attenuated signal $s(z)$ that forms an OCT A-scan is given as

$$s(z) = Kr_S(z)e^{-2\alpha \int_{z_0}^{z} r_S(w)dw} \quad (8)$$

where K is a possible coefficient of conversion remaining from the OCT postprocessing, then

$$\int_{z}^{\infty} s(u)du = -\frac{K}{2\alpha}\int_{z}^{\infty} -2\alpha r_S(u) e^{-2\alpha \int_{z_0}^{u} r_S(w)dw} du = -\frac{K}{2\alpha}\left[e^{-2\alpha \int_{z_0}^{u} r_S(w)dw} \right]_{z}^{\infty} = \frac{K}{2\alpha} e^{-2\alpha \int_{z_0}^{z} r_S(w)dw} \quad (9)$$

so that

$$\frac{s(z)}{2\int_{z}^{\infty} s(u)du} = \alpha r_S(z) = HD\{s(z)\}. \quad (10)$$

where HD is an operator that transforms a given signal $s(z)$ into its compensated (i.e., unattenuated) form. Similar to the situation in ultrasound imaging, the local attenuation can be estimated from the above equation, suggesting that it is possible to automatically compensate OCT images without requiring the estimation of model parameters (α and K). The attenuation coefficient α remains in equation 10, but the extracted quantity $\alpha r_S(z)$ is a nondecaying profile that allows the display of unshadowed images. The actual reflectivity profile $r_S(z)$ could be estimated through measurement of α, but this is difficult to achieve experimentally and beyond the scope of the proposed study. In the following section, the approach devised by Hughes and Duck will be applied to clinically captured spectral-domain OCT images of the ONH and its ease of application will be addressed. Note that a practical implementation of equation 10 is given in the Appendix.

Application. Spectral-domain OCT volumes were acquired from the right eye of four human subjects (subject 1: male, 36 years old, optical refraction −6.75/−2.00 D × 100°, axial length 26.99 mm; subject 2: male, 30 years old, optical refraction −2.50/−0.25 D × 124°, axial length 24.69 mm; subject 3: female, 33 years old, optical refraction −2.25/−0.25 D × 160°, axial length 24.98 mm; and subject 4: female, 30 years old, optical refraction −1.75 DS; axial length, 23.73 mm) with a commercially available device (Spectralis; Heidelberg Engineering, Heidelberg, Germany). Imaging was performed at Moorfields Eye Hospital, London, where regional ethics committee approval was obtained. All subjects gave informed consent and were treated in accordance with the Declaration of Helsinki. Each scan pattern comprised 97 horizontal B-scans acquired over a 15° × 15° retinal window, with 768 A-scans (of 496 pixels each) per B-scan. Each B-scan was acquired nine times and was averaged for speckle noise reduction. It should be emphasized that the proposed theory is valid for both time-domain and spectral-domain OCT applications, but was tested only with spectral-domain OCT, as this technology has been shown to be more reliable, producing fewer artifacts.[38]

Intralayer Contrast. To verify that the proposed algorithm can remove blood vessel shadows from ONH images, we computed the intralayer contrast for multiple tissues of the ONH region, namely PS, choroid, retinal pigment epithelium (RPE), outer nuclear layer (ONL), outer plexiform layer (OPL) and LC, before and after application of the proposed compensation algorithm. The intralayer contrast was defined as

$$\text{Intralayer contrast} = \left| \frac{I_1 - I_2}{I_1 + I_2} \right| \quad (11)$$

where I_1 is the mean image intensity of a region of interest (ROI; 5 × 1 pixels) located within an arbitrarily selected shadow-free region of a given tissue layer, and I_2 is that within a neighboring shadowed region of the same tissue layer. By definition, the intralayer contrast varies between 0 and 1, with values close to 0 indicating the

absence of blood vessel shadows, and values closer to 1 indicating shadowing.

Contrast Enhancement

In digital image processing, image compression (not to be confused with data compression to reduce digital storage) is commonly performed to reduce the dynamic range of pixel intensities, hence allowing simultaneous observation of strong and weak signals within a given image. For instance, logarithmic or n^{th} root compression are frequently applied to raw OCT images for better visualization of all ocular structures in a clinical setting.[39] Conversely, image expansion is commonly performed to increase the dynamic range of pixel intensities (e.g., through exponentiation or I, where I is the pixel intensity and n is the exponent) for contrast enhancement purposes. This latter transformation enhances the ability of edge detection and segmentation algorithms to identify boundaries between adjacent tissue layers. This is of interest in morphometric and biomechanical studies of the ONH. However, direct application of pixel intensity exponentiation for contrast enhancement is not always feasible in regions of strong attenuation (such as at high depth or behind a blood vessel), since the transformed signal will show more pronounced shadows or complete loss of signal. Accordingly, we propose that the use of the aforementioned compensation algorithm, which will restore signal in strongly attenuated ONH image regions, is a necessary first step in contrast enhancement. Exponentiation can therefore be applied to OCT images immediately after compensation (from equation 10) for contrast enhancement as

$$[\mathrm{HD}\{I(z)\}]^n = \frac{I^n(z)}{\left[2\int_z^\infty I(u)du\right]^n} \quad (12)$$

and this transformation will be compared to exponentiation without compensation or $I^n(z)$. For the sake of completeness, we will also study the following transformation (exponentiation then compensation)

$$\mathrm{HD}\{I^n(z)\} = \frac{I^n(z)}{2\int_z^\infty I^n(u)du}. \quad (13)$$

For simplicity, we will use $n = 2$ for the rest of this report, with the use of a larger exponent being discussed later. Finally, the proposed algorithms will be applied to B-scans from the aforementioned ONH volumes captured with spectral-domain OCT.

Interlayer Contrast. To verify that the proposed algorithms can enhance contrast from OCT images, we computed the interlayer contrast across multiple tissue boundaries of the ONH (i.e., PS/choroid, ONL/OPL, inner nuclear layer [INL]/inner plexiform layer [IPL], and LC/PT), before and after application of the proposed contrast-enhancement algorithms. Similarly to the intralayer contrast, the interlayer contrast was defined as

Table 1. Intralayer Contrast

	Baseline				Compensation				Exponentiation				Compensation + Exponentiation				Exponentiation + Compensation			
	1	2	3	4	1	2	3	4	1	2	3	4	1	2	3	4	1	2	3	4
Image 1																				
PS	.73	.70	.70	.52	.23	.14	.10	.14	.95	.94	.93	.79	.45	.28	.19	.22	.28	.13	.01	.16
Choroid	.76	.55	.40	.51	.01	.10	.03	.02	.96	.84	.68	.81	.02	.36	.05	.04	.01	.24	.17	.05
RPE	.86	.93	.94	.95	.30	.38	.46	.34	.99	.99	.99	.99	.56	.60	.64	.66	.38	.11	.36	.20
ONL	.69	.90	.57	.88	.12	.04	.11	.05	.93	.99	.85	.99	.25	.04	.29	.02	.45	.32	.37	.34
OPL	.83	.86	.43	.77	.11	.17	.09	.20	.98	.98	.74	.93	.23	.30	.20	.35	.04	.60	.35	.52
Image 2																				
PS	.68	.49	.75	.42	.07	.04	.24	.03	.93	.82	.96	.72	.14	.08	.46	.06	.23	.08	.26	.02
Choroid	.52	.81	.77	.64	.01	.33	.16	.19	.82	.98	.96	.91	.01	.59	.27	.34	.13	.47	.12	.12
RPE	.88	.81	.86	.94	.36	.38	.24	.20	.99	.98	.98	.99	.64	.60	.38	.36	.24	.22	.20	.12
ONL	.73	.92	.66	.50	.06	.14	.08	.26	.95	.99	.92	.83	.14	.32	.16	.41	.47	.39	.26	.46
OPL	.77	.91	.55	.87	.04	.06	.03	.29	.96	.99	.88	.99	.08	.12	.02	.56	.29	.10	.24	.62
Image 3																				
PS	.55	.52	.67	.52	.07	.08	.11	.16	.85	.81	.92	.76	.16	.15	.23	.19	.04	.05	.06	.11
Choroid	.57	.63	.51	.75	.18	.19	.09	.25	.86	.91	.84	.95	.35	.36	.10	.45	.42	.21	.24	.35
RPE	.88	.82	.91	.93	.46	.48	.45	.40	.99	.97	.99	.99	.76	.67	.77	.72	.49	.38	.41	.31
ONL	.77	.91	.75	.90	.02	.18	.23	.07	.96	.99	.95	.99	.02	.37	.39	.37	.24	.43	.61	.73
OPL	.77	.79	.69	.88	.04	.01	.06	.10	.96	.96	.94	.99	.09	.02	.12	.19	.43	.16	.34	.50
Image 4																				
LC	.98	.55	.50	.66	.25	.05	.16	.33	.99	.85	.81	.94	.49	.11	.33	.63	.18	.19	.38	.46
Image 5																				
LC	.96	.92	.95	.71	.29	.30	.06	.13	.99	.99	.99	.95	.55	.56	.11	.30	.77	.25	.45	.09
Image 6																				
LC	.98	.79	.87	.77	.36	.10	.17	.29	.99	.97	.99	.95	.65	.20	.35	.44	.44	.20	.21	.26
Mean	.77	.76	.69	.72	.16	.17	.15	.19	.94	.94	.90	.91	.31	.31	.28	.35	.30	.25	.28	.30
Mean ± SD		.74 ± .16				.17 ± .12				.92 ± .07				.31 ± .21				.28 ± .17		

The intralayer contrast was computed (between shadowed and shadow-free regions) for multiple tissue layers of the ONH and for six different images (images 1–3 were located away from the optic disc and images 4–6 within) in each of four human subjects. Application of the proposed compensation algorithm significantly reduced the intralayer contrast (baseline vs. compensation) and thus decreased the visibility of the blood vessel shadows present in the initial images (see Fig. 1).

Exponentiation significantly increased the intralayer contrast in all cases and thus increased the visibility of blood vessel shadows (see Fig. 2C). Combining exponentiation with compensation (rightmost two data groups) significantly reduced the intralayer contrast from that obtained from the baseline image, hence indicating successful shadow removal. However, in both cases, the decrease was not as high as that obtained with the use of compensation only.

$$\text{Interlayer contrast} = \left|\frac{I_3 - I_4}{I_3 + I_4}\right| \quad (14)$$

where I_3 is the mean image intensity of an ROI ($5 \times b$ pixels, with b representing the thickness of the considered tissue layer in pixels) located within an arbitrary shadow-free region of a given tissue layer, and I_4 is that within a shadow-free region of its adjacent tissue layer. By definition, the interlayer contrast varies between 0 and 1. A value close to 0 indicates that the boundary of interest is poorly detectable, whereas that close to 1 indicates a highly detectable boundary.

Statistics

Results are reported as the mean ± SD. Statistical analyses were performed by using unpaired Student's *t*-test (MatLab; The MathWorks, Natick, MA), with $P < 0.05$ indicating statistical significance.

Results

Blood Vessel Shadow Removal

The intralayer contrast decreased consistently for each eye and for each layer after application of the compensation algorithm, indicating successful shadow removal in each layer (Table 1). On average, the intralayer contrast significantly decreased from 0.74 ± 0.16 to 0.17 ± 0.12 ($P < 0.001$). Recall that an intralayer contrast close to 0 indicates complete shadow removal. This is confirmed by inspection of two images (away from and within the optic disc) before and after application of the proposed compensation algorithm (Fig. 1). It is clear that the shadows were indeed removed and that deeper tissue layers, such as the PS and the LC, were restored and more visible, confirming that attenuation was successfully corrected. This is also consistent with the flattening of the lateral pixel intensity passing through both shadowed and shadow-free regions of the PS after compensation (Figs. 2A, 2B).

Contrast Enhancement

On average, all three contrast enhancement techniques (exponentiation, compensation+exponentiation, and exponentiation+compensation) significantly increased the interlayer contrast from 0.48 ± 0.22 to 0.72 ± 0.28, 0.89 ± 0.05, and 0.88 ± 0.07, respectively ($P < 0.001$; Table 2). The results suggest that the tissue boundaries will become more easily detectable when using automated segmentation techniques. We also noted that the combined use of compensation and exponentiation resulted in higher interlayer contrasts than

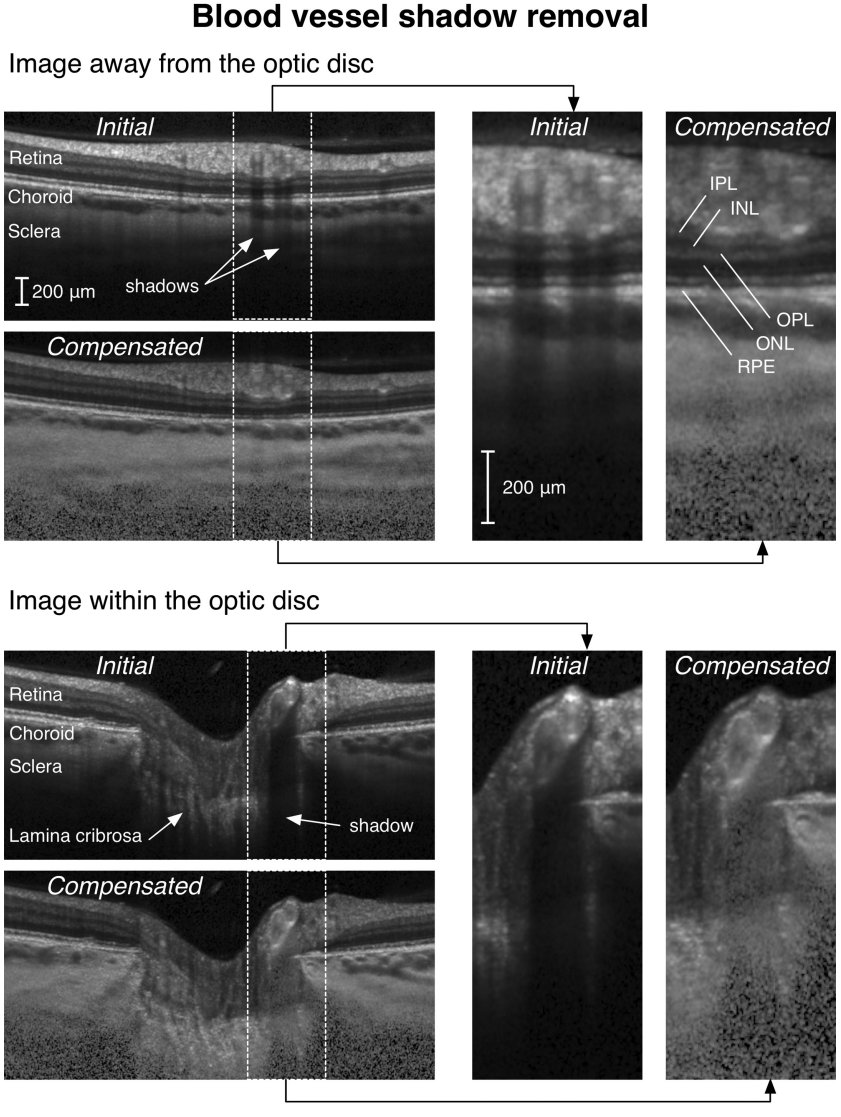

Figure 1. Two spectral-domain OCT images (within and away from the optic disc) are shown before and after application of the proposed compensation algorithm. After compensation, blood vessel shadows were removed, and structures at high depth (i.e., the PS and LC) became more visible. Attenuation was therefore successfully corrected. Zoomed-in views of the shadowed regions are shown for each image for better illustration.

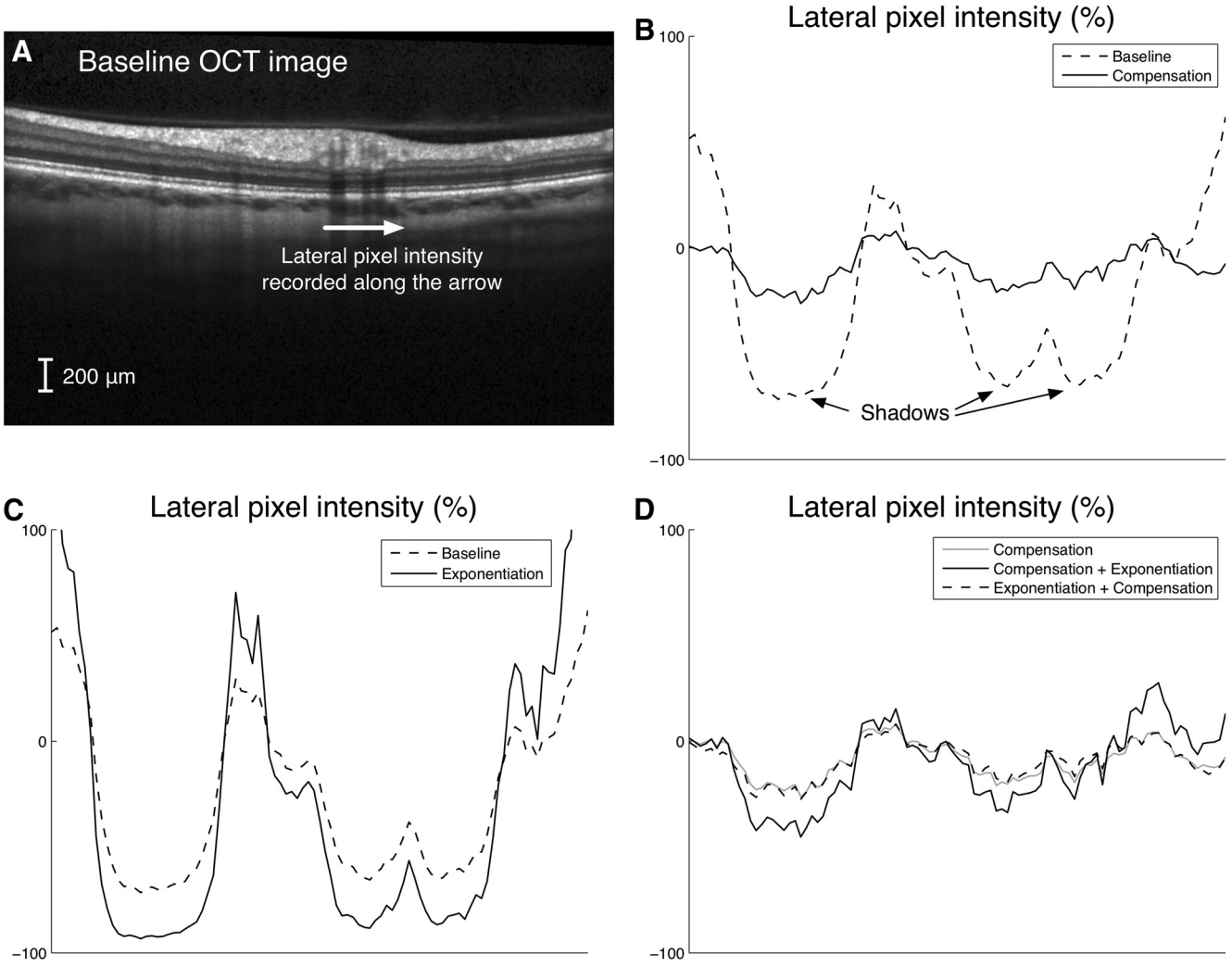

Figure 2. (**A**) Lateral pixel intensity (percentage difference from mean value along line) was recorded along a line in the PS, as indicated by the *arrow* superimposed on a baseline B-scan captured with spectral-domain OCT. (**B**) Baseline versus compensation. In the baseline OCT image, the lateral pixel intensity exhibits regions of low magnitude, which correspond to the presence of blood vessel shadows. After compensation, the lateral pixel intensity flattens and becomes more uniform, suggesting successful shadow removal. (**C**) Baseline versus exponentiation. When exponentiation (with $n = 2$) is applied to the baseline OCT image, it has the adverse effect of generating higher intensity gradients, implying that blood vessel shadows are more noticeable. (**D**) Compensation versus compensation+exponentiation. Application of combined compensation and exponentiation (in either sequence) to the baseline OCT image successfully renders the lateral pixel intensity more uniform (as opposed to that obtained from the baseline OCT image). For this specific case, exponentiation+compensation performed as well as compensation (via similar intralayer contrasts), but compensation+exponentiation performed slightly worse (via a slightly higher intralayer contrast).

those obtained with exponentiation only (Table 2, Fig. 3). In some cases, exponentiation failed to improve only the contrast at the PS–choroid and the LC–PT boundaries, which is consistent with the fact that the PS and LC are highly attenuated tissues and that compensation is a necessary step for contrast enhancement. On the other hand, the use of compensation with exponentiation did not provide any improvements at the INL–IPL and ONL–OPL tissue boundaries. Finally, examination of the image pixel intensity versus depth within the LC further illustrates the advantages of the combined exponentiation/compensation effects on contrast enhancement (Fig. 4). We observed considerable improvement when exponentiation was combined with compensation (either way) as opposed to exponentiation only. Note that noncompensated signals (baseline and exponentiation) exhibited an exponential decay in the LC, indicating the presence of strong attenuation.

Effects of Contrast Enhancement on Blood Vessel Shadow Removal

We aimed to understand the effects of contrast enhancement on blood vessel shadow removal (or decreased intralayer contrast). On average, only two of the three proposed contrast-enhancement techniques (exponentiation+compensation, and compensation+exponentiation) were able to significantly decrease the intralayer contrast, from 0.74 ± 0.16 to 0.31 ± 0.21 and 0.28 ± 0.17, respectively ($P < 0.001$; Table 1). However, these values were still higher than the one obtained with compensation only (0.17 ± 0.12). This finding is illustrated by Figure 2D which presents lateral pixel intensity through both the shadowed and shadow-free regions before and after contrast enhancement with comparison to compensation only. In the compensation+exponentiation case, the lateral pixel intensity flattened (suggesting shadow removal) after contrast enhancement but not as strongly as it did with compensation only.

TABLE 2. Interlayer Contrast

	Baseline				Compensation				Exponentiation				Compensation + Exponentiation				Exponentiation + Compensation			
	1	2	3	4	1	2	3	4	1	2	3	4	1	2	3	4	1	2	3	4
Image 1																				
PS/choroid	.11	.04	.48	.10	.67	.58	.77	.54	.11	.10	.78	.20	.88	.85	.96	.82	.83	.80	.95	.80
ONL/OPL	.75	.61	.63	.58	.75	.62	.62	.59	.96	.88	.89	.87	.96	.90	.88	.88	.96	.91	.88	.89
INL/IPL	.57	.62	.63	.70	.60	.61	.60	.65	.85	.89	.90	.94	.87	.89	.88	.91	.88	.89	.89	.92
Image 2																				
PS/choroid	.58	.21	.51	.16	.81	.65	.82	.60	.88	.49	.80	.41	.97	.90	.98	.87	.97	.88	.97	.86
ONL/OPL	.82	.70	.69	.79	.82	.70	.71	.75	.98	.94	.93	.97	.98	.94	.94	.96	.98	.94	.94	.96
INL/IPL	.51	.61	.56	.53	.50	.58	.58	.54	.81	.89	.85	.83	.81	.88	.86	.86	.82	.88	.90	.88
Image 3																				
PS/choroid	.39	.07	.48	.11	.76	.58	.74	.50	.77	.02	.79	.23	.96	.85	.95	.77	.96	.82	.93	.74
ONL/OPL	.72	.73	.75	.68	.71	.76	.75	.64	.95	.94	.96	.93	.94	.96	.96	.90	.94	.96	.96	.90
INL/IPL	.65	.50	.67	.62	.63	.43	.61	.60	.91	.78	.92	.90	.90	.71	.89	.89	.91	.73	.90	.91
Image 4																				
PS/choroid	.10	.24	.57	.38	.73	.60	.80	.72	.42	.49	.86	.72	.95	.87	.97	.94	.93	.83	.97	.92
ONL/OPL	.73	.67	.73	.62	.72	.68	.61	.64	.95	.93	.95	.91	.94	.94	.88	.92	.95	.94	.89	.93
INL/IPL	.57	.61	.52	.64	.57	.59	.48	.57	.87	.88	.79	.90	.86	.87	.75	.86	.87	.88	.77	.88
LC/PT	.43	.54	.20	.28	.75	.51	.65	.48	.78	.71	.37	.48	.96	.82	.90	.76	.88	.81	.81	.61
Image 5																				
PS/choroid	.08	.05	.38	.07	.61	.58	.75	.53	.01	.02	.73	.18	.88	.86	.95	.81	.82	.81	.94	.75
ONL/OPL	.72	.76	.71	.69	.72	.76	.70	.69	.94	.96	.95	.93	.94	.96	.94	.94	.95	.96	.93	.95
INL/IPL	.57	.60	.59	.63	.55	.59	.58	.61	.86	.88	.86	.90	.85	.88	.85	.88	.86	.89	.86	.90
LC/PT	.53	.06	.11	.13	.78	.50	.69	.64	.84	.14	.19	.29	.97	.78	.92	.90	.92	.71	.89	.81
Image 6																				
PS/choroid	.22	.23	.34	.21	.71	.67	.67	.59	.65	.58	.53	.52	.94	.92	.90	.87	.93	.92	.87	.87
ONL/OPL	.68	.64	.70	.74	.67	.64	.67	.70	.92	.91	.94	.96	.92	.91	.92	.94	.92	.91	.91	.95
INL/IPL	.49	.64	.57	.52	.49	.60	.60	.53	.79	.91	.84	.78	.79	.88	.86	.79	.80	.88	.89	.81
LC/PT	.17	.43	.44	.43	.60	.48	.58	.76	.07	.75	.67	.75	.88	.82	.85	.95	.79	.82	.75	.94
Mean	.49	.45	.53	.45	.67	.60	.66	.61	.72	.67	.78	.69	.91	.87	.90	.87	.89	.86	.89	.86
Mean ± SD		.48 ± .22				.63 ± .09				.72 ± .28				.89 ± .05				.88 ± .07		

The interlayer contrast was computed across different tissue boundaries of the ONH (i.e. PS-choroid, ONL-OPL, INL-IPL, and LC-PT for six different images (images 1–3 are located away from the optic disc and images 4–6 within) in each of four human subjects. On average, all techniques significantly increased the interlayer contrast from that computed from the baseline images. Combined compensation and exponentiation (rightmost two data groups) produced the largest increases, especially at the LC-PT and PS-choroid boundaries.

Conversely, exponentiation only significantly increased the intralayer contrast (0.92 ± 0.07), resulting in more pronounced blood vessel shadows (Fig. 3, third row). Figure 2C also illustrates that point where we observed large deflections in lateral pixel intensity from a shadowed region to a shadow-free region. This deflection was in fact higher than the one observed from the initial (or baseline) image.

DISCUSSION

In this study, we have proposed several algorithms to enhance OCT images of the ONH by removing blood vessel shadows, improving tissue visibility at high depth, and enhancing image contrast to facilitate detection and segmentation of tissue boundaries. These algorithms can be implemented easily (see the Appendix), and do not require any prior segmentation, delineation, or identification of the attenuated regions by the user. This study is a preliminary step toward automated segmentation of the ONH, which will ultimately lead to quantification of ONH biomechanics in vivo, with the hope that an improved understanding of the pathogenesis, diagnosis, and risk-profiling of glaucoma can be achieved.

To the best of our knowledge, inclusion of an attenuation term has not been considered and assessed by studies on OCT theory, and we suggest that it is a necessary step to achieve automated segmentation of the ONH. The fact that the Hughes and Duck algorithm,[33] originally developed for use with ultrasound, can be used for attenuation correction in OCT images implies that OCT theory will benefit from the developments that have been achieved in pulse–echo techniques research, such as the one proposed here.

Compensation provided two major improvements with respect to the baseline OCT images. First, it successfully removed blood vessel shadows (as demonstrated by the significant decrease in intralayer contrast; see Table 1 and Fig. 1), which will facilitate segmentation through the use of simple automated algorithms. This achievement has a direct implication for automated detection of, for instance, retinal pathologies and glaucoma. Second, compensation increased tissue visibility at substantial depth, particularly that of the LC and PS. Both are the main load-bearing tissues of the eye in the region of the ONH, and it has been suggested that either biomechanical or morphologic features of these tissues could serve as risk indicators for glaucoma.[5,11,40] The robustness of the OCT-based measurements performed on these tissues should be dramatically improved after application of the proposed compensation algorithm.

This compensation algorithm can be used with both time- and spectral-domain OCT, and can be used on existing images—for example, from longitudinal studies with OCT to improve measurements on the LC and/or PS. A

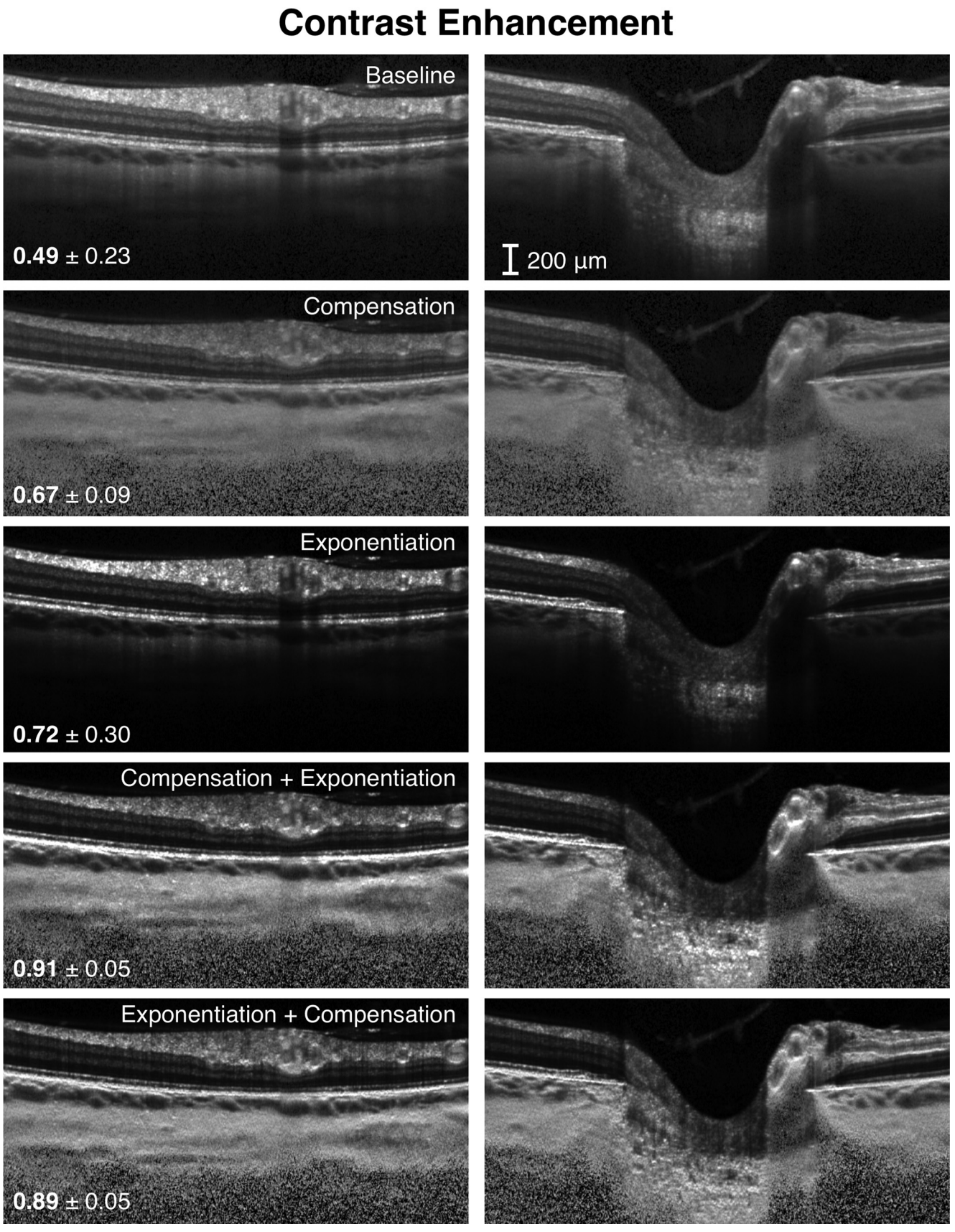
Contrast Enhancement
Baseline
0.49 ± 0.23
200 µm
Compensation
0.67 ± 0.09
Exponentiation
0.72 ± 0.30
Compensation + Exponentiation
0.91 ± 0.05
Exponentiation + Compensation
0.89 ± 0.05

FIGURE 3

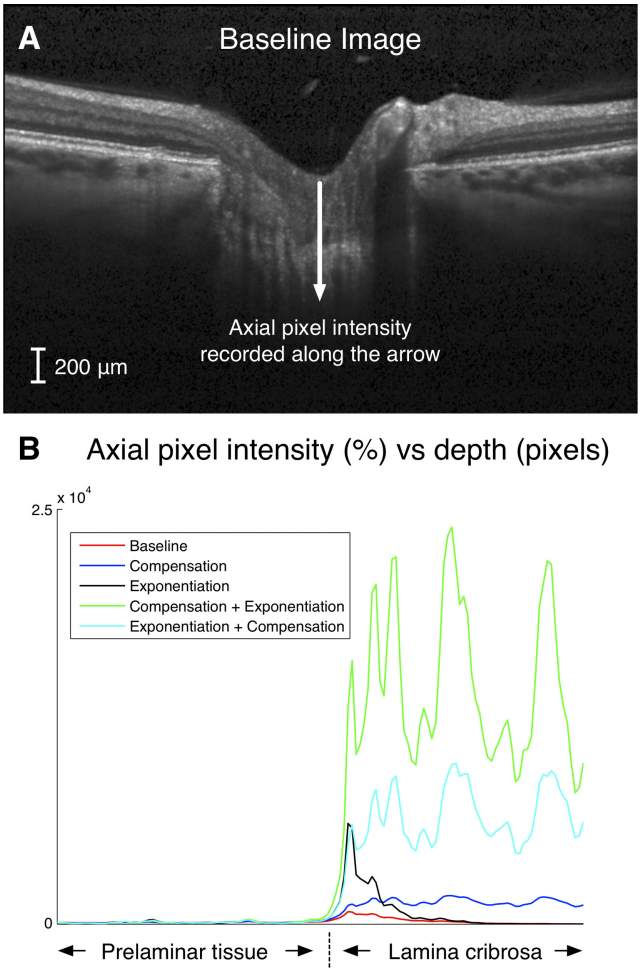

FIGURE 4. **(A)** Axial pixel intensity (percentage difference from the mean value along a line) was recorded as a function of depth in the PT and LC as indicated by the *arrow* superimposed on a baseline B-scan taken within the optic disc. **(B)** Axial pixel intensity for different OCT images (baseline, compensation, exponentiation, compensation+compensation, exponentiation+compensation). All transformations (compared with the baseline) improved the percentage difference in axial pixel intensity at the PT–LC interface. In the LC, the baseline and exponentiation signals exhibited attenuation (exponential decay of the axial pixel intensity) as opposed to the three other signals. Although the exponentiation signal exhibited a large jump in intensity between the PT and LC regions, the signal quickly attenuated with depth. Overall, combining compensation and exponentiation provided the most satisfying results with no attenuation and higher interlayer contrasts (Table 2).

recent study has already looked into laminar changes with an acute change in IOP.[18] Future such studies will likely benefit from this work.

In the second section of our work, we enhanced the contrast of the OCT images. This approach, when combined with compensation, considerably increased the intralayer contrast (Fig. 3, Table 2), producing more easily detectable tissue boundaries (Fig. 4). However if enhancement was directly applied to the raw OCT images without compensation, shadows became more apparent (when compared to baseline images), and deeper tissues (such as the LC and PS) were less visible. In short, compensation appears to be a necessary first step for contrast enhancement of OCT images. When compared to compensated images, compensated and contrast-enhanced images exhibited slightly higher intralayer contrasts, indicating more visible blood vessel shadows. Nevertheless, this intralayer contrast was still significantly lower than that obtained from the baseline images. This reveals a tradeoff between complete blood vessel shadow removal and contrast enhancement. Finally, we mention that the interlayer contrast further increases for an exponent $n > 2$ (data not shown), and it may be tempting to pursue this approach. However, the use of a higher exponent usually generated more speckle noise in the images, which could eventually compromise the application of edge-detection and segmentation algorithms. Further work is needed to evaluate this impact once segmentation algorithms are combined with the image processing algorithms proposed in this study.

Several limitations of this work should be pointed out. While detection of the anterior boundaries of the LC and PS should be considerably facilitated by the proposed algorithms, detection of the posterior boundaries of these tissues still may not be straightforward. An approach, called enhanced depth imaging, allows users to scan the deeper tissues of the ONH.[41–43] This is achieved either by altering the distance between the OCT device and the patient's eye or the distance between the reference mirror and the beam splitter. With this technique, an inverted image of the tissues is created, with increased signal at higher depth. Enhanced depth imaging has recently been incorporated into the image acquisition software for the Spectralis device (Heidelberg Engineering), but was not available at the time of image acquisition for this study. We hope that the algorithms proposed in this study can be combined with enhanced depth imaging OCT to provide more accurate posterior boundary detection and thus thickness measurements of deeper target tissues.

Another shortcoming of this study is that, when we introduced attenuation into the governing OCT equations, we assumed that attenuation was linearly proportional to reflectivity through the coefficient α. However, α could be nonconstant, and knowledge of its spatial distribution in each individual tissue layer of the ONH could improve the accuracy of the compensation. Unfortunately, this will be difficult to achieve in practice and implies a priori knowledge of the tissue boundaries, which is precisely one of the goals of preprocessing to facilitate segmentation. This field remains unexplored in OCT research.

Furthermore, for direct application of compensation to OCT images, the approach of Hughes and Duck must be discretized (as described in the Appendix). While taking this step, the denominator sum in equations A3, A4, and A5 will eventually become small at high depth, giving abnormally high pixel intensities and higher noise at high depth (see

FIGURE 3. The interlayer contrast (a measure of intensity jump between tissue layers) was computed away from (left column) and within (right column) the optic disc for the following cases: baseline, compensation, exponentiation, compensation1exponentiation, exponentiation1compensation. The value of the interlayer contrast (a measure of intensity jump between tissue layers) was computed away from (*left column*) and within (*right column*) the optic disc for the following cases: baseline, compensation, exponentiation, compensation+exponentiation, exponentiation+compensation. The value of the intralayer contrast (subject 1; mean ± SD taking into account all tissue layers, as summarized in Table 2) is indicated at the bottom left of each image. It was noted that compensation, when combined with exponentiation, provided the best interlayer contrasts (*bottom two rows*). Exponentiation (*third row*) did increase the interlayer contrast; however, blood vessel shadows became more pronounced (as demonstrated in Fig. 2C) and tissue visibility at high depth was reduced. This result suggests that compensation is an essential step for successful contrast enhancement of OCT images.

Figs. 1, 3). This was not a major issue for the purpose of this study, as most tissues of interest can be centered within a certain field of view. Nevertheless, to overcome the problem, future work could consider a correction factor at high depth to be introduced in the discretized equations (A3–A5).

In conclusion, to enhance OCT images, we have proposed a series of algorithms that can be applied to both time- and spectral-domain OCT images. These algorithms provided significant improvements with respect to baseline OCT images by eliminating blood vessel shadows, increasing the visibility of deeper tissues such as the LC and PS, and enhancing contrast for future use with segmentation algorithms to better detect tissue boundaries and thus provide better thickness measurements. This study can be developed further by improving the proposed theory through knowledge of scattering properties of the ocular tissues and by adapting recent progress in ultrasound imaging to OCT. Since morphologic and biomechanical features of the ONH are potential risk indicators for glaucoma, this study provides a framework toward collection of such data in a robust manner.

Acknowledgments

The authors thank Felicia Ikeji and Ed White from Moorfields Eye Hospital who captured the OCT images used in the study.

References

1. Resnikoff S, Pascolini D, Etya'ale D, et al. Global data on visual impairment in the year 2002. *Bull World Health Organ*. 2004;82:844–851.
2. Quigley HA, Addicks EM, Green WR, Maumenee AE. Optic nerve damage in human glaucoma. II. The site of injury and susceptibility to damage. *Arch Ophthalmol.* 1981;99:635–649.
3. Leske MC. Open-angle glaucoma: an epidemiologic overview. *Ophthalmic Epidemiol.* 2007;14:166–172.
4. Sigal IA, Roberts MD, Girard MJA, Burgoyne CF, Downs JC. *Biomechanical Changes of the Optic Disc: Ocular Disease: Mechanisms and Management.* New York: Elvesier; 2009.
5. Burgoyne CF, Downs JC, Bellezza AJ, Suh JK, Hart RT. The optic nerve head as a biomechanical structure: a new paradigm for understanding the role of IOP-related stress and strain in the pathophysiology of glaucomatous optic nerve head damage. *Prog Retin Eye Res.* 2005;24:39–73.
6. Sigal IA, Ethier CR. Biomechanics of the optic nerve head. *Exp Eye Res.* 2009;88:799–807.
7. Downs JC, Roberts MD, Burgoyne CF. Mechanical environment of the optic nerve head in glaucoma. *Optom Vis Sci.* 2008;85:425–435.
8. Sander EA, Downs JC, Hart RT, Burgoyne CF, Nauman EA. A cellular solid model of the lamina cribrosa: mechanical dependence on morphology. *J Biomech Eng.* 2006;128:879–889.
9. Newson T, El-Sheikh A. Mathematical modeling of the biomechanics of the lamina cribrosa under elevated intraocular pressures. *J Biomech Eng.* 2006;128:496–504.
10. Edwards ME, Good TA. Use of a mathematical model to estimate stress and strain during elevated pressure induced lamina cribrosa deformation. *Curr Eye Res.* 2001;23:215–225.
11. Sigal IA. Interactions between geometry and mechanical properties on the optic nerve head. *Invest Ophthalmol Vis Sci.* 2009;50:2785–2795.
12. Roberts MD, Liang Y, Sigal IA, et al. Correlation between local stress and strain and lamina cribrosa connective tissue volume fraction in normal monkey eyes. *Invest Ophthalmol Vis Sci*. 2010;51:295–307.
13. Girard MJ, Downs JC, Burgoyne CF, Suh JK. Peripapillary and posterior scleral mechanics-part I: development of an anisotropic hyperelastic constitutive model. *J Biomech Eng.* 2009;131:051011.
14. Bellezza AJ, Hart RT, Burgoyne CF. The optic nerve head as a biomechanical structure: initial finite element modeling. *Invest Ophthalmol Vis Sci.* 2000;41:2991–3000.
15. Grytz R, Meschke G, Jonas JB. The collagen fibril architecture in the lamina cribrosa and peripapillary sclera predicted by a computational remodeling approach. *Biomech Model Mechanobiol.* 2011;10(3):371–382.
16. Fujimoto JG. Optical coherence tomography: introduction. In: Bouma BE, Tearney GJ, eds. *Handbook of Optical Coherence Tomography*. London: Informa Healthcare; 2001.
17. Strouthidis NG, Grimm J, Williams GA, Cull GA, Wilson DJ, Burgoyne CF. A comparison of optic nerve head morphology viewed by spectral domain optical coherence tomography and by serial histology. *Invest Ophthalmol Vis Sci*. 2010;51:1464–1474.
18. Agoumi Y, Sharpe GP, Hutchison DM, Nicolela MT, Artes PH, Chauhan BC. Laminar and prelaminar tissue displacement during intraocular pressure elevation in glaucoma patients and healthy controls. *Ophthalmology*. 2011;118:52–59
19. Yang H, Downs JC, Girkin C, et al. 3-D histomorphometry of the normal and early glaucomatous monkey optic nerve head: lamina cribrosa and peripapillary scleral position and thickness. *Invest Ophthalmol Vis Sci.* 2007;48:4597–4607.
20. Yang H, Downs JC, Sigal IA, Roberts MD, Thompson H, Burgoyne CF. Deformation of the normal monkey optic nerve head connective tissue after acute IOP elevation within 3-D histomorphometric reconstructions. *Invest Ophthalmol Vis Sci.* 2009;50:5785–5799.
21. Burgoyne CF, Yang H, Downs JC. Clinical cupping: laminar and prelaminar components. *The Glaucoma Book*: New York: Springer; 2010:185–194.
22. Sigal IA, Yang H, Roberts MD, Burgoyne CF, Downs JC. IOP-induced lamina cribrosa displacement and scleral canal expansion: an analysis of factor interactions using parameterized eye-specific models. *Invest Ophthalmol Vis Sci*. 2011;52:1896–1907.
23. Yang H, Thompson H, Roberts MD, Sigal IA, Downs JC, Burgoyne CF. Deformation of the early glaucomatous monkey optic nerve head connective tissue after acute IOP elevation within 3-D histomorphometric reconstructions. *Invest Ophthalmol Vis Sci*. 2011;52:345–363.
24. Downs JC, Roberts MD, Sigal IA. Glaucomatous cupping of the lamina cribrosa: a review of the evidence for active progressive remodeling as a mechanism. *Exp Eye Res*. 2010 Aug 11 [Epub ahead of print].
25. Inoue R, Hangai M, Kotera Y, et al. Three-dimensional high-speed optical coherence tomography imaging of lamina cribrosa in glaucoma. *Ophthalmology.* 2009;116:214–222.
26. Skolnik M. *Introduction to Radar Systems*. 3rd ed. New York: McGraw-Hill; 2002.
27. Hodges RP. *Underwater Acoustics*: *Analysis*, *Design and Performance of Sonar*. West Sussex, UK: Wiley; 2010.
28. Mari JM, Blu T, Matar OB, Unser M, Cachard C. A bulk modulus dependent linear model for acoustical imaging. *J Acoust Soc Am.* 2009;125:2413–2419.
29. Tang MX, Mari JM, Wells PN, Eckersley RJ. Attenuation correction in ultrasound contrast agent imaging: elementary theory and preliminary experimental evaluation. *Ultrasound Med Biol.* 2008;34:1998–2008.
30. Mari J, Hibbs K, Stride E, Eckersley R, Tang M. An approximate nonlinear model for time gain compensation of amplitude modulated images of ultrasound contrast agent perfusion. *IEEE Trans Ultrason Ferroelectr Freq Control*. 2010;57(4):818–829.
31. Borchert O, Behaimanot K, Glasmachers A. Directional borehole radar calibration. *J Appl Geophys.* 2009;67:352–360.
32. Chang S, Flueraru C, Mao Y, Sherif S. Attenuation compensation for optical coherence tomography imaging. *Optics Communications.* 2009;282:4503–4507.
33. Hughes DI, Duck FA. Automatic attenuation compensation for ultrasonic imaging. *Ultrasound Med Biol.* 1997;23:651–664.
34. Andersen PE, Jorgensen TM, Thrane L, Tycho A, Yura HT. Modeling light-tissue interaction in optical coherence tomography systems. In: Drexler W, Fujimoto JG eds. *Optical Coherence*

Tomography: *Technology and Applications*. New York: Springer; 2008.
35. Izatt JA, Rollins AM, Ung-Arunyawee R, Yazdanfar S, Kulkarni MD. System integration and signal/image processing. In: Bouma BE, Tearney GJ, eds. *Handbook of Optical Coherence Tomography*. London: Informa Healthcare; 2001.
36. Izatt JA, Choma MA. Theory of optical coherence tomography. In: Drexler W, Fujimoto JG, eds. *Optical Coherence Tomography*: *Technology and Applications.* New York: Springer; 2008.
37. van de Hulst HC. *Light Scattering by Small Particles*. Mineola, NY: Dover Publications; 1981.
38. Sayanagi K, Sharma S, Yamamoto T, Kaiser PK. Comparison of spectral-domain versus time-domain optical coherence tomography in management of age-related macular degeneration with ranibizumab. *Ophthalmology.* 2009;116:947–955.
39. Dubois A, Boccara AC. Full-field optical coherence tomography. In: Drexler W, Fujimoto JG eds. *Optical Coherence Tomography*: *Technology and Applications*. New York: Springer; 2008.
40. Ethier CR. Scleral biomechanics and glaucoma: a connection? *Can J Ophthalmol.* 2006;41:9–12, 14.
41. Yeoh J, Rahman W, Chen F, et al. Choroidal imaging in inherited retinal disease using the technique of enhanced depth imaging optical coherence tomography. *Graefes Arch Clin Exp Ophthalmol*. 2010;248(12):1719–1728.
42. Spaide RF, Koizumi H, Pozzoni MC. Enhanced depth imaging spectral-domain optical coherence tomography. *Am J Ophthalmol.* 2008;146:496–500.
43. Imamura Y, Fujiwara T, Margolis R, Spaide RF. Enhanced depth imaging optical coherence tomography of the choroid in central serous chorioretinopathy. *Retina.* 2009;29:1469–1473.

APPENDIX

Discretization of the Proposed Algorithms

The proposed algorithms are summarized by equation 10 for compensation and equations 12 and 13 for contrast enhancement. They need to be discretized for direct application to a given set of images (or B-scans) captured with either time- or spectral-domain OCT. In the following, we assume that a B-scan can be simply defined as $I(i, j)$, where I is the pixel intensity value for a pixel located in the ith row and jth column, with $i \in [1; p]$ and $j \in [1; q]$, and where $p \times q$ represents the total number of pixels. Here, we follow the matrix convention, meaning that both i and j indexes start from 1 at the top left corner of the image. It is important to emphasize that the B-scans must be obtained in raw format. For example, the Heidelberg Spectralis commonly applies the following transformation (referred as compression in this article) to better visualize all structures within a given image.

$$I_{compr}(i, j) = 255 \sqrt[4]{I(i, j)}. \quad (A1)$$

If this is the case, images must be transformed back to their initial raw format as

$$I(i, j) = \left(\frac{I_{compr}(i, j)}{255}\right)^4. \quad (A2)$$

To compensate an image, one must apply the aforementioned operator HD to each A-scan for a given image or B-scan I. Since an A-scan is defined for a given index j, as $I(i, j \in [1; q])$, the newly compensated image J can be computed as

$$J(i, j) = \mathrm{HD}\{I(i, j)\} = \frac{I(i, j)}{2\sum_{k=i}^{p} I(k, j)\Delta z} \quad (A3)$$

where $\Delta z = 1$, if we work in the image (not physical) coordinate system. Accordingly, since our contrast enhancement algorithms simply exponentiate the pixel intensity, either before or after compensation, we obtain the contrast-enhanced images K and L as

$$K(i, j) = [\mathrm{HD}\{I(i, j)\}]^n = \frac{I^n(i, j)}{\left(2\sum_{k=i}^{p} I(k, j)\right)^n} \quad (A4)$$

and

$$L(i, j) = \mathrm{HD}\{I^n(i, j)\} = \frac{I^n(i, j)}{2\sum_{k=i}^{p} I^n(k, j)}. \quad (A5)$$

Note that all these operations require the discretization of an infinite integral from equation 10. Since a given OCT image is not infinite depthwise, the proposed algorithms will degenerate at substantial depth, as addressed in the Discussion section.

Although the above equations can be implemented by the user in any programming language (e.g., C/C++, Fortran), we propose a simple implementation in the software (MatLab; The MathWorks), using the following command for equations A3, A4, and A5, respectively, as

```
J = I./ (flipud (cumtrapz(flipud(I))));
```
(A6)

```
K = (I./ (flipud (cumtrapz
                  (flipud(I))))).^n;
```
(A7)

```
L = (I.^n)./ (flipud(cumtrapz
                  (flipud(I.^n))));
```
(A8)

where I is a $p \times q$ matrix representing a given B-scan, and J, K, and L are the enhanced images. At this stage, it is interesting to compress the images with equation A3 or other logarithmic transformation for visualization purposes only.